ANNALS OF THE NEW YORK ACADEMY OF SCIENCES

Original Article

Uncertainty of runoff sensitivity to climate change in the Amazon River basin

Alejandra M. Carmona,[1,2,3] 🆔 Maik Renner,[1] Axel Kleidon,[1] and Germán Poveda[4]

[1]Biospheric Theory and Modelling Group, Max Planck Institute for Biogeochemistry, Jena, Germany. [2]Department of Innovation, Constructora Conconcreto, Medellín, Colombia. [3]Faculty of Engineering and Architecture, Institución Universitaria Colegio Mayor de Antioquia, Medellín, Colombia. [4]Department of Geosciences and Environment, Universidad Nacional de Colombia, Medellín, Colombia

Address for correspondence: Alejandra M. Carmona, Director of Innovation at Constructora Conconcreto, Department of Innovation, Constructora Conconcreto, Carrera 43A No. 18 Sur 135, Sao Paulo Plaza, 050022 Medellín, Antioquia, Colombia. amcarmona@conconcreto.com

We employ the approach of Roderick and Farquhar (2011) to assess the sensitivity of runoff (R) given changes in precipitation (P), potential evapotranspiration (E_p), and other properties that change the partitioning of P (n) by estimating coefficients that predict the weight of each variable in the relative change of R. We use this framework using different data sources and products for P, actual evapotranspiration (E), and E_p within the Amazon River basin to quantify the uncertainty of the hydrologic response at the subcatchment scale. We show that when estimating results from the different combinations of datasets for the entire river basin (at Óbidos), a 10% increase in P would increase R on average 16%, while a 10% increase in E_p would decrease R about 6%. In addition, a 10% change in the parameter n would affect the hydrological response of the entire basin around 5%. However, results change from catchment to catchment and are dependent on the combination of datasets. Finally, results suggest that enhanced estimates of E and E_p are needed to improve our understanding of the future scenarios of hydrological sensitivity with implications for the quantification of climate change impacts at the regional (subcatchment and subbasin) scale in Amazonia.

Keywords: Budyko framework; runoff sensitivity; evapotranspiration; catchment hydrology; Amazon River basin

Introduction

The Amazon River basin (ARB) is one of the few environmental tipping points of the Earth's system. In this context, the term *tipping point* is employed to define a critical threshold at which a small perturbation can qualitatively alter the state or development of a system.[1–3] Indeed, there is a strong body of the literature showing the likely die-back of the Amazon rainforest owing to the positive feedbacks between reduction in rainfall, temperature increase, and deforestation.[4,5] Such transition would not be gradual but sudden where certain critical thresholds are surpassed, such as a 4 °C increase in temperature or a 40% increase in deforestation.

At those critical points, the forest ceases to behave as a carbon sink and becomes a source, such that the forest collapses and is replaced by a savanna-type vegetation.[1–3,6–14] On the other hand, in terms of hydrological regulation,[15] it shows that catchments in the ARB can shift from a regulated to a nonregulated state when deforestation surpasses 30–40% of the forest cover. Then, floods and droughts become exacerbated, therefore, amplifying the variance of hydrological extremes, owing to the loss of regulation capacity in the "forest reservoir." Such a shift in the hydroclimatic and ecological functioning of the whole ARB could have long-term consequences for the climatic system worldwide since the hydrological, climatological, and biogeochemical dynamics

Table 1. Summary of possible dataset combinations

Dataset combination	Precipitation P (mm yr^{-1})	Actual evapotranspiration E (mm yr^{-1})	Potential evapotranspiration E_p (mm yr^{-1})	Maximum number of subcatchments
1	HYBAM	MPI	Hargreaves	146
2	HYBAM	MPI	Priestley and Taylor	146
3	HYBAM	GLEAM	Hargreaves	146
4	HYBAM	GLEAM	Priestley and Taylor	146
5	GPCC	MPI	Hargreaves	146
6	GPCC	MPI	Priestley and Taylor	146
7	GPCC	GLEAM	Hargreaves	146
8	GPCC	GLEAM	Priestley and Taylor	146
9	HYBAM	P–R	Hargreaves	100
10	HYBAM	P–R	Priestley and Taylor	100
11	GPCC	P–R	Hargreaves	100
12	GPCC	P–R	Priestley and Taylor	100

play an important role in regulating water, energy, and carbon budgets not only in South America but also are key hydroclimatic drivers at continental and global scales.

Multiple studies have dealt with the estimation of the long-term mean surface water balance of the ARB since it provides a coherent framework to understand the spatiotemporal dynamics of hydrologic fluxes across river basins (see Table 1 of Ref. 16). In general, these studies have addressed the water balance for the entire river basin (at Óbidos gauging station) and few of them report near steady-state conditions or almost exact water balance closure. However, as pointed out by Builes-Jaramillo and Poveda,[16] such results of perfect closure are mostly influenced by the dependence of datasets in estimations of evapotranspiration (E), that is, E derived from precipitation (P) products. Another source for the lack of a perfect closure of the long-term water balance is the possible existence of trends in a series of rainfall and river flows that violate the mean value theorem, and thus $R \neq P-E$. Studies by Greve *et al.*[17] and Moussa *et al.*[18] have provided insights to deal with this problem. At smaller spatial scales in the ARB (subcatchment scale), calculations of the closure of the water balance present major discrepancies, especially between observed data and reanalysis datasets.[16]

Thus, estimation of hydrologic fluxes is dependent on the chosen datasets in terms of their quality, accuracy, record lengths, and the presence of trends and changes. These inconsistencies in water balance estimations affect runoff calculations and the quantification of the combined impacts from climate variability, anthropogenic climate change, and deforestation and land use changes, given the complex nature of hydroclimatological processes. Thus, a deeper understanding of the spatiotemporal dynamics of river basins is required. This analysis could include the coupling between water and energy budgets, considering that water cycle in Amazonia is sensitive to perturbations caused by human-related activities[19] and it is also driven by diverse natural climate variability phenomena, including the El Niño–Southern Oscillation (ENSO)[20–26] and changes in sea surface temperatures in the Tropical North Atlantic, among others.[27–29]

The theoretical framework introduced by Budyko provides a functional relationship to understand the coupling between water and energy budgets in river basins. It has been used to address fundamental questions in hydrology, such as water availability and management, runoff prediction, and climate change studies.[17,30–43] It has also been used at various spatial and temporal scales to perform diagnostic analyses of the long-term mean annual water balances in catchments and to study the interactions between hydroclimate, soil, vegetation, and topography.[44–50]

This study aims to: (1) estimate the closure of the surface water balance across subcatchments of

Figure 1. Location of the six major river basins within the Amazon River basin.

the ARB comparing different datasets of P, E, and E_p; (2) employ Budyko's framework using Roderick and Farquhar's approach[35] to assess the sensitivity of runoff (R) in the ARB, given changes in climatic variables (P) and potential evapotranspiration (E_p), as well as in other properties that affect the partitioning of P, represented by the parameter n, by estimating the sensitivity coefficients that analytically predict the weight of each variable (P, E_p, and n) in the relative change of R across the ARB and its six major subbasins. In particular, we aim to (3) investigate the spatial variability of three sensitivity coefficients across the major subcatchments of the ARB and to (4) quantify the uncertainty in the estimation of the sensitivity coefficients given the currently available datasets on the water budget components of the ARB catchments.

Materials and methods

Study area and datasets

The ARB is the largest river basin in the world and constitutes a singular biogeographic, physiographic, hydrological, and climatic entity rich in biodiversity. It is located in tropical South America, between 5°N and 20°S, and 80°W and 50°W, approximately. It drains an area of about 6,700,000 km^2 across important portions of Brazil, Bolivia, Colombia, Ecuador, Peru, Venezuela, Suriname, and French Guyana. Its main channel has a length of 6280 km with a mean annual flow of 209,000 m^3 s^{-1} at its farthest downstream gauging station, Óbidos.[51] This river basin can be divided into 146 subcatchments, which, in turn, can be grouped into six major river subbasins (Fig. 1): Solimões, Purus, Negro, Madeira,

Tapajós, and Xingú. There are approximately 15,000 tributaries in the ARB, including the Madeira River, which is considered the longest one (3380 km), and the Negro River with the largest discharge of up to 100,000 $m^3 s^{-1}$ (Ref. 52).

Since one of our goals is to estimate the closure of the surface water balance across the ARB and to quantify the uncertainty in the estimation of the sensitivity coefficients comparing different datasets, we used at least two sources of data for each hydrological variable, except for runoff. P [LT^{-1}] and river discharges, Q [$L^3 T^{-1}$], were obtained from the Observation Service SO-HYBAM (formerly the Environmental Research Observatory ORE-HYBAM), available at http://www.ore-hybam.org/. Precipitation data were also used from the Global Precipitation Climatology Centre (GPCC), calculated from global station data.[53] River discharge records, Q, were transformed into runoff, R [LT^{-1}], considering that $R = Q/A$, with A [L^2] being the drainage area of each subcatchment. Data regarding actual E [LT^{-1}] were obtained from a global monitoring network combined with meteorological observations and remote sensing data, compiled by the Max Planck Institute for Biogeochemistry (MPI)[54] as well as from the Global Land Evaporation Amsterdam Model (GLEAM), a set of algorithms that separately estimate the different components of land evapotranspiration.[55,56] We also used actual E estimated from the water balance equation ($E = P–R$) with data from precipitation (HYBAM and GPCC) and observed runoff. For E_p [LT^{-1}], we also used two different methods. First, we used the often-applied Hargreaves equation:[57]

$$E_p = 0.0023 (T_{max} - T_{min})^{0.5} (T_{mean} + 17.8) R_a, \quad (1)$$

where T_{max}, T_{min}, and T_{mean} are the maximum, minimum, and mean air temperatures (°C), respectively, and R_a is the extraterrestrial radiation or solar radiation at the top of the atmosphere. We used this equation following Trabucco and Zomer[58] who compared four different temperature-based methods for E_p and concluded that for South America, this model is one of the most suitable ways to estimate E_p. The Hargreaves equation was estimated using station data of daily minimum and maximum temperatures from the Climatic Research Unit

(CRU).[59] Finally, E_p was also estimated using the Priestley–Taylor equation:[60]

$$E_p = \alpha \left(\frac{\Delta}{\Delta + \gamma} \right) (R_n - G), \quad (2)$$

with the Priestley–Taylor empirical parameter $\alpha = 1.26$, the slope of the saturation vapor pressure curve (Δ) as a function of temperature, the psychrometric constant γ, net radiation R_n, and ground heat flux G. We used annual average data from the remote sensing product of the Surface Radiation Budget (SRB; https://eosweb.larc.nasa.gov/project/srb/srb_table),[61] at 1-degree resolution for net radiation and surface temperature to estimate Δ. The ground heat flux was neglected since we use annual mean data.

All variables (P, R, E, and E_p) were available at a monthly temporal resolution (mm month^{-1}) from January 1984 to December 2007, thus covering 24 years of data. Also, P and E were available for 146 subcatchments, while Q was available only for 100 of them. For this reason, the analysis requiring calculations of runoff was only carried out for this subset of subcatchments. Table 1 summarizes the 12 possible combinations of datasets used in this study.

The water balance equation

In a now-classic paper, Dooge[62] stated that the fundamental business of hydrology is to solve the water balance equation at a wide range of spatial and temporal scales. It is the differential equation representing the conservation of mass within a control volume defined by a river basin, and expressed as:[63]

$$\frac{dS}{dt} = P(t) - R(t) - E(t), \quad (3)$$

where $S(t)$ represents water storage in soils and groundwater as a function of time, $P(t)$ and $E(t)$ denote, respectively, P and actual E in the river basin, and $R(t)$ denotes the surface runoff at the basin's outlet. Integration of Eq. (3) over long time periods (15–20 years), the change in water storage with time (left-hand side) becomes negligible when compared with the other terms of the equation. In the long term, the right-hand side terms $P(t)$, $E(t)$, and $R(t)$ converge to their long-term mean values provided that the probability distribution function of the variables is stationary, according to the mean value theorem. Therefore, Eq. (3) becomes:

$$\bar{R} = \bar{P} - \bar{E}. \quad (4)$$

The terms in Eq. (4) have units of $[\text{LT}^{-1}]$, and thus the river basin drainage area, A, becomes the scaling factor of runoff to obtain the long-term mean river streamflow, Q $[\text{L}^3\text{T}^{-1}] = R$ $[\text{LT}^{-1}]$ A $[\text{L}^2]$. Hereinafter, we leave out the bars in Eq. (4) to denote the long-term annual mean values of the respective terms.

The Budyko framework

This theory relates actual E with two variables representing the water and energy budgets, respectively: P and E_{p} for river basins over long timescales, and thus $E = f(P, E_{\text{p}})$. Such a relationship is constrained by two physical limits: (1) $E \to E_{\text{p}}$ as $P \to \infty$ (energy-limited wet environments); and (2) $E \to P$ as $E_{\text{p}} \to \infty$ (water-limited dry environments). Budyko[64] went on to propose that $E/P = f(E_{\text{p}}/P)$, where the nondimensional variable E_{p}/P is referred to as the aridity index (Φ), and, therefore, the previous two limits become: (1) $E/P \to \Phi$ as $\Phi \to 0$ (E is energy-limited); and (2) $E/P \to 1$ as $\Phi \to \infty$ (E is water-limited). The ratio E/P can be considered a measure of the long-term mean annual water balance in a river basin, since it is the fraction of the water falling as precipitation that is partitioned into evapotranspiration. On the other hand, Φ is a measure of the long-term mean climate-related energy availability to water availability. Small values of Φ ($\Phi < 1$) are associated with humid catchments where precipitation is significant, and the energy supply is the limiting factor for evapotranspiration. Conversely, large values of Φ ($\Phi > 1$) are found in arid regions where precipitation is low, and evapotranspiration is limited by water supply.

In this paper, we used the Budyko framework to study the relative change in runoff in a given catchment as a function of relative changes in two climatic variables (P and E_{p}) and in other properties that affect the partitioning of P, represented by the parameter n. For this purpose, we employ the approach by Roderick and Farquhar[35] and the following equations (see Ref. 35 for their derivation):

$$\frac{dR}{R} = \left[\frac{P}{R}\left(1 - \frac{\partial E}{\partial P}\right)\right]\frac{dP}{P} - \left[\frac{E_{\text{p}}}{R}\frac{\partial E}{\partial E_{\text{p}}}\right]\frac{dE_{\text{p}}}{E_{\text{p}}}$$

$$- \left[\frac{n}{R}\frac{\partial E}{\partial n}\right]\frac{dn}{n}. \tag{5}$$

The three terms in the brackets of Eq. (5) are referred to as runoff sensitivity coefficients, such that:

$$\varepsilon_P = \left[\frac{P}{R}\left(1 - \frac{\partial E}{\partial P}\right)\right], \tag{6}$$

$$\varepsilon_{E_{\text{p}}} = \left[\frac{E_{\text{p}}}{R}\frac{\partial E}{\partial E_{\text{p}}}\right], \tag{7}$$

$$\varepsilon_n = \left[\frac{n}{R}\frac{\partial E}{\partial n}\right]. \tag{8}$$

In these equations, the water balance constraint implies that the runoff sensitivity coefficients of P and E_{p} add up to one, as $\varepsilon_P + \varepsilon_{E_{\text{p}}} = 1$.[65] Also, in Eqs. (5)–(8), n represents other factors that change the partitioning of P between E and R.[35] That is, n captures all factors that are known to influence runoff generation, such as topography, soils, and vegetation and other aspects like changes in precipitation intensity or changes in the spatial distribution, and/or seasonal timing of P and E_{p}. For example, Yang and Yang[66] suggested that n increases in catchments with the amount of water available for E, thus, a large value of n indicates that there is sufficient green water available for E to achieve close to its maximum value under any climatic condition. For Eq. (8), n was fitted for each subcatchment and each combination of datasets using interannual data and the Budyko-type equation by Yang *et al.*[67]

The formulation by Roderick and Farquhar[35] assumes steady-state water balance conditions and, therefore, calculations require a timescale whereby changes in catchment storage are small relative to the magnitude of fluxes. For this reason, monthly values of P, E, E_{p}, and R were converted to long-term means. Also, before any further analysis was carried out, we confirmed that the 12 possible combinations of datasets (mentioned above) follow the Budyko framework. This was done by plotting the location of each dataset in the Budyko space (Φ versus E/P). We found that not only this framework holds when using the proposed datasets but also most subcatchments are located in the humid space (where $\Phi < 1$), as it was thoroughly shown for the catchments of the ARB by Carmona *et al.*[39] These results are not shown here for the sake of brevity. We also calculated the Spearman's rank correlation coefficient between Φ and E/P for each dataset. This test
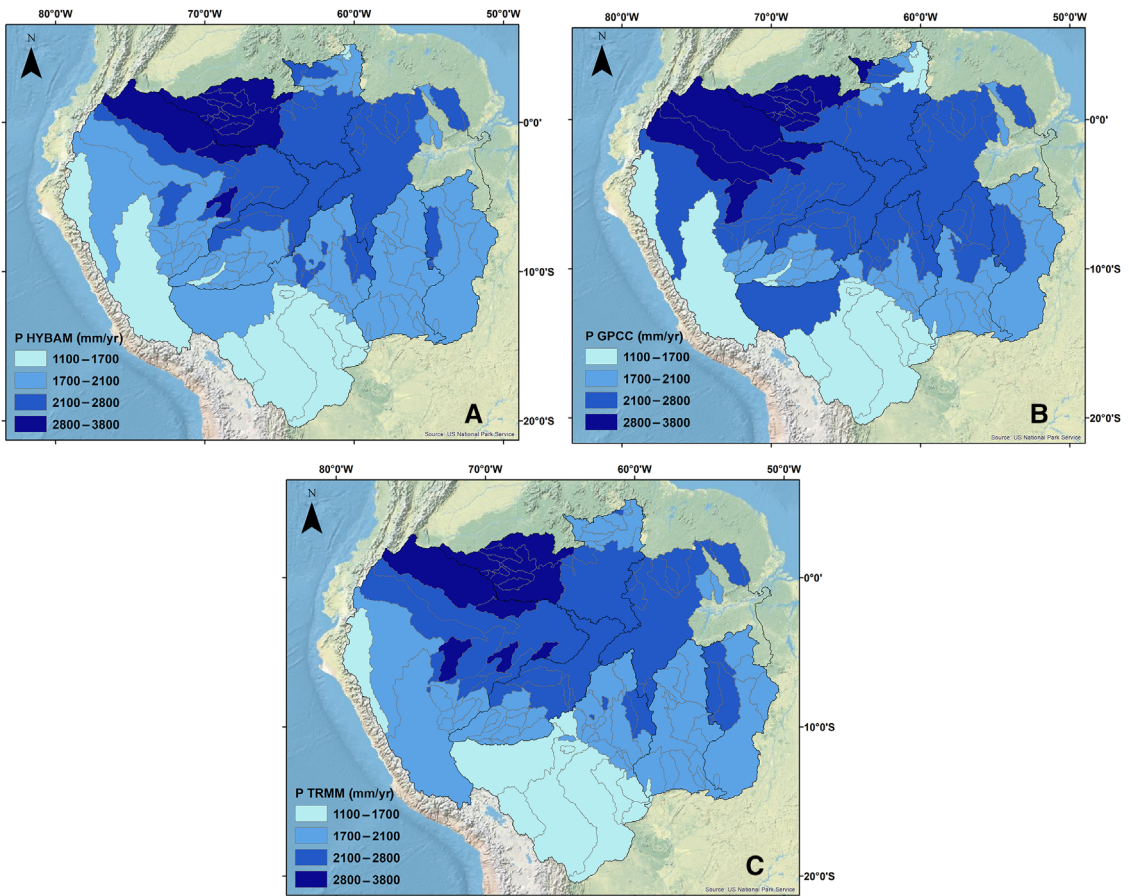
Figure 2. Long-term mean annual rainfall maps for the 146 catchments of the Amazon River basin, estimated with different datasets: HYBAM 1984–2007 (A), GPCC 1984–2007 (B), and TRMM 2001–2009 (C).

evaluates how well the relationship between two variables can be described using a monotonic function, with values from $+1$ (perfect positive association) to -1 (perfect negative association). The closer ρ is to zero, the weaker the association between the ranks. Results show moderate ($+0.5$) to strong ($+0.7$) correlations between our variables (E_p/P and E/P). This suggests that all combinations of datasets are useful for the analysis presented in this manuscript. However, according to these results, the best combinations are #1 (P HYBAM – E MPI – E_p Hargreaves, $\rho = 0.95$) and #5 (P GPCC – E MPI – E_p Hargreaves, $\rho = 0.96$), and the worst is #12 (P GPCC– $E = P$–R– E_p Priestley–Taylor, $\rho = 0.50$). We also found that among all, the weakest correlations are obtained when using E estimated from the water balance equation (P–R) as in combinations 9–12 in Table 1.

Finally, we follow the approach by Jung *et al.*[68] to quantify the relative contribution of uncertainty. Therefore, we carried out a multilinear regression linking the differences between the ensembles of datasets for each subcatchment using the following equations:

$$\Delta \varepsilon_p = a^* \Delta P + b^* \Delta E + c^* \Delta E_p, \qquad (9)$$

$$\Delta \varepsilon_{E_p} = a^* \Delta P + b^* \Delta E + c^* \Delta E_p, \qquad (10)$$

$$\Delta \varepsilon_n = a^* \Delta P + b^* \Delta E + c^* \Delta E_p. \qquad (11)$$

In these equations, ΔP, ΔE_p, and ΔE are the difference of each dataset of a variable (P, E, or E_p) and the mean value of all combinations of datasets for that variable. For example, ΔP is the difference of each precipitation product (HYBAM or GPCC) and the mean value of P using all precipitation products
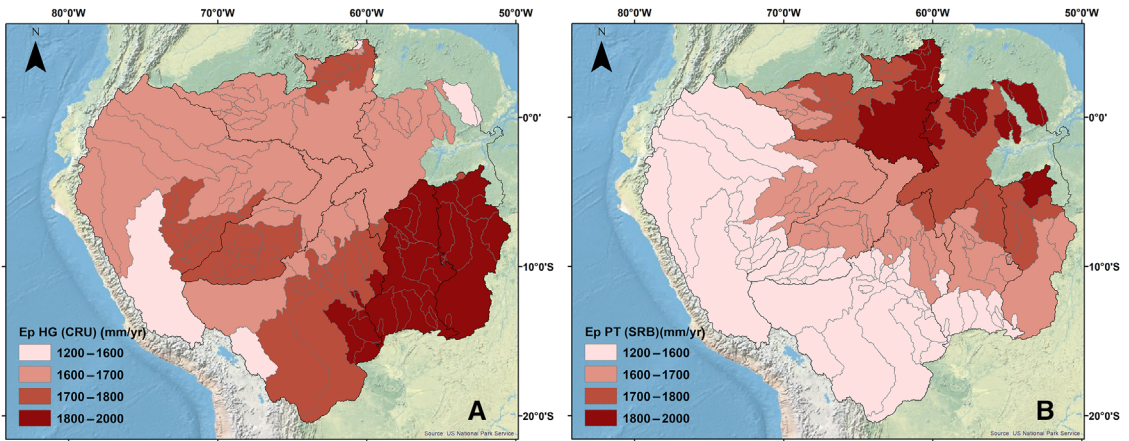
Figure 3. Long-term mean annual potential evapotranspiration (E_p) maps for the 146 catchments of the Amazon River basin, estimated using the data of mean monthly temperature range and mean monthly extraterrestrial radiation from the CRU (A) and the surface radiation budget (SRB) (B).

(i.e., $\Delta P = P$ HYBAM – P mean). Also, $\Delta\varepsilon_p$, $\Delta\varepsilon_{E_p}$, and $\Delta\varepsilon_n$ are the difference of each sensitivity coefficient (in Eqs. 6–8) of each dataset combination and the overall mean of the ensemble of 12 dataset combinations in Table 1. Equations (9)–(11) are used to estimate the relative contribution of each variable to each sensitivity coefficient in each subcatchment. Also, *a*, *b*, and *c* are the coefficients of the multilinear regression.

Results

Recalling the objectives of the present study, we discuss below the spatial distribution of P, E_p, and E, and their variability across the ARB. The following subsection is focused on the estimation of the water balance closure using different measurements and estimations of P and E and observed R to determine which combination of datasets yields the best runoff estimates. Finally, we estimate the sensitivity coefficients that analytically predict the weight of P, E_p, and n in the relative change of R across the ARB. We also explore their spatial variability across the major subcatchments and quantify the uncertainty in their calculation.

Spatial variability of P
Long-term mean annual rainfall fields estimated with HYBAM and GPCC data are shown in Figure 2 (panels A and B, respectively). For spatial comparison purposes, data from the Tropical Rainfall Mea-

suring Mission (TRMM[69]) for the period spanning from 2001 to 2009 were also plotted (Fig. 2C). The three maps show similar regional precipitation patterns, indicating that the long-term mean annual precipitation in the ARB ranges from 1100 mm yr^{-1} to up to 3800 mm yr^{-1}, and that the highest annual precipitation intensities occur in the Colombian Amazon (northwestern region), while the lowest precipitation rates are witnessed in Peru (western region), Bolivia (southwestern region), and some parts of Brazil (southeastern region). To quantify the differences or similarities between the HYBAM and GPCC data, the relative difference between these datasets was estimated. These relative differences are of the order of 10% (−10% to 10%) in 75% of the 146 subcatchments, while in 25% subcatchments, this difference is higher than 10% (ranging from −20% to 66%).

Spatial variability of E_p
Figure 3 presents the long-term mean annual fields of E_p estimated using the Hargreaves equation (panel A) with data from the CRU, and the Priestley–Taylor equation (panel B) using data from the SRB. Unlike for precipitation, this figure shows that both datasets produce very different spatial estimates, only coinciding in a few catchments located toward the center of the ARB. The Hargreaves method locates the highest E_p values (up to 1885 mm yr^{-1}) over the eastern part of the ARB decreasing westward, while the Priestley–Taylor
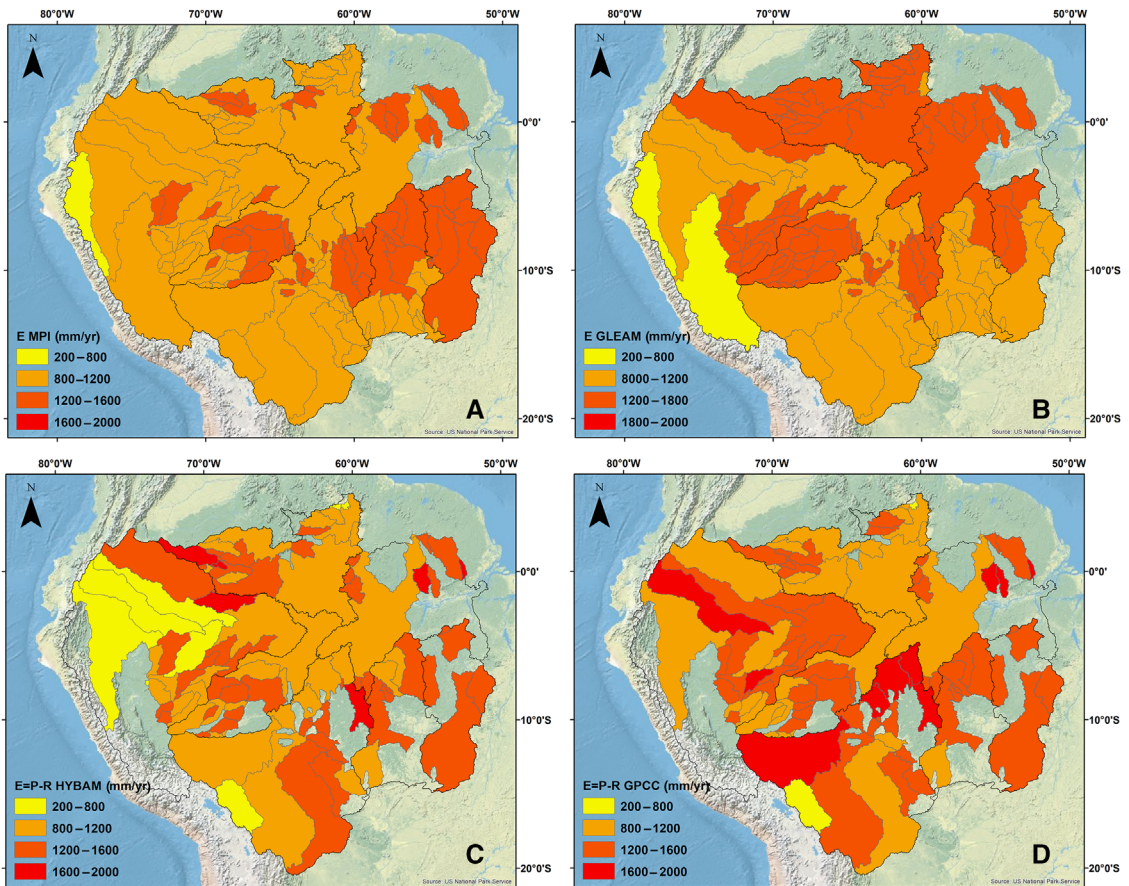
Figure 4. Spatial distribution of long-term mean annual actual evapotranspiration (*E*) in the Amazon River basin with four different datasets: (A) MPI, (B) GLEAM, (C) difference between long-term mean *P* from HYBAM and observed *R*, and (D) difference between long-term mean *P* from GPCC and observed runoff.

estimates locate the highest E_p values toward the northeast, decreasing systematically toward the southwest. It should be kept in mind that values in Figure 3A were calculated using temperature data and mean monthly extraterrestrial radiation, while values in Figure 3B were calculated using short- and longwave radiation. Estimated relative differences between datasets are about 10% (−10% to 10%) in 55% of the 146 subcatchments, while for 45% of them, the difference is higher than 10%, ranging from −20% to 26%.

Spatial variability of actual E

Figure 4 presents the long-term mean annual fields of actual *E* obtained from MPI (Fig. 4A) and GLEAM (Fig. 4B). These two datasets produce quite different spatial patterns in the long-term mean

annual actual *E*, although both coincide in that the region with the lowest values of *E* located near Perú and Bolivia (Fig. 4A and B). For comparison purposes in those subcatchments where *Q* data were available, *E* was also estimated using the water balance equation as $E = P–R$ using precipitation data from HYBAM (Fig. 4C) and GPCC (Fig. 4D). Figure 4 shows that GLEAM estimates of *E* exhibit a similar pattern to E_p estimates using the Priestley–Taylor equation, showing the highest values toward the northeast. This is mostly because GLEAM also uses the Priestley–Taylor equation to calculate E_p based on the observations of surface net radiation and near-surface air temperature. Also, Figure 4 shows that MPI estimates show less spatial variability compared with results using GLEAM or the water balance closure.
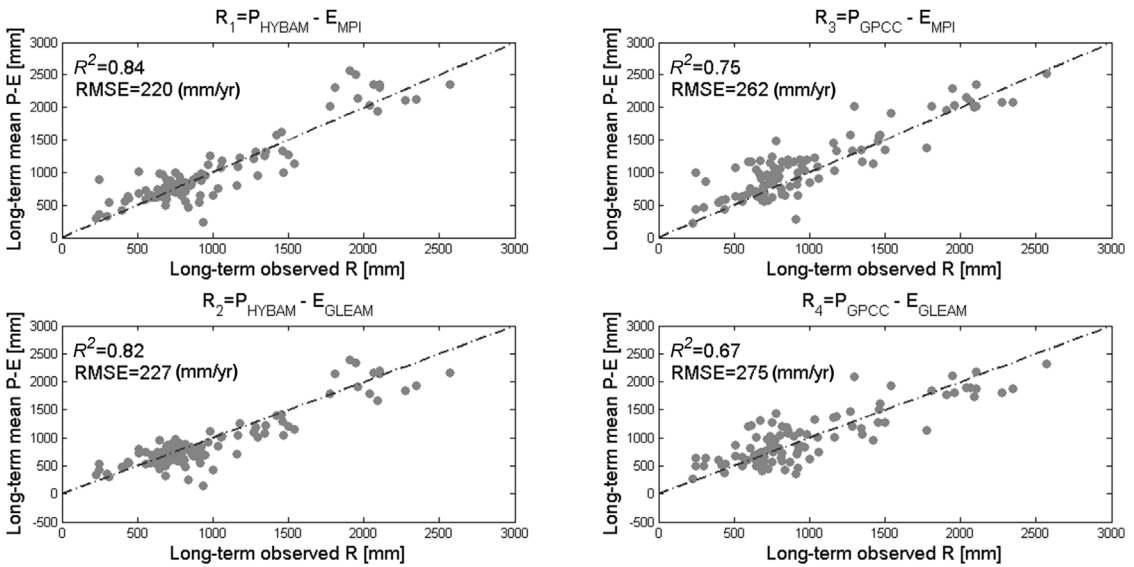
Figure 5. Comparison of estimated *R* using four combinations of datasets of *P* and *E* versus observed runoff.

Relative differences between datasets were estimated using *E* from the water balance (*P*–*R*) as a reference, in order to compare results between MPI and GLEAM. These results show a possible disagreement between remote sensing actual *E* and the water budget at the climatological mean. Results from the relative difference between *E* from MPI and *E* calculated with *P* from HYBAM are among 10% in 55% of the subcatchments, while in 45% of catchments, these differences are higher than 10% (from −36% to 136%). For *E* from GLEAM and *E* with *P* from HYBAM, in 48% of the subcatchments, differences are among 10%, while in 52% of subcatchments, differences are higher than 10% (from −26% to 154%). When using *E* calculated with *P* from GPCC, these percentages change as follows: (1) for *E* from MPI, in 39% of the subcatchments, differences are among 10%, and in 61% of them, differences are higher than 10% (ranging from −41% to 238%), and (2) for *E* from GLEAM, in 34% of the subcatchments, differences are among 10%, and in 66% of them, differences are higher than 10% (ranging from −45% to 210%). In general, differences seem to be smaller when using *E* from MPI compared with *E* from GLEAM. Also, relative differences increase when using *E* calculated using *P* data from GPCC.

Closure of the water balance
The water balance closure was examined for 100 subcatchments of the ARB in terms of the estimation of *R*, using four combinations of *P* and *E* datasets: (1) *P* Hybam + *E* MPI (R_1); (2) *P* Hybam + *E* Gleam (R_2); (3) *P* GPCC + *E* MPI (R_3); and (4) *P* GPCC + *E* Gleam (R_4). Then, the values of estimated *R* = *P*–*E* were compared with the observed values of *R*. Figure 5 plots *R* estimated using each combination of datasets with observed *R*. In this Figure, each dot represents one catchment. The coefficient of determination (R^2) and the root-mean-square error (RMSE) are used as a measure of how well observed outcomes are replicated by each model. As shown in Figure 5, results for the water balance closure of the 100 subcatchments indicate that the lowest RMSE values are obtained when calculating *R* using *P* from HYBAM with actual *E* from MPI (RMSE = 220 mm yr^{-1}) and GLEAM (RMSE = 227 mm yr^{-1}). It is worth noticing in Figure 5 that high RMSE results are almost independent of the *E* estimate but better with *P* from HYBAM than from GPCC.

We also quantified deviations of *R* catchment per catchment as the relative difference between estimated and observed runoff. Assuming we accept a 10% difference, for the entire ARB (at Óbidos), the

Table 2. Percentage of catchments with 10% or less than 10% difference between observed and estimated *R* using the four combinations of datasets

Runoff models	RMSE (mm yr^{-1})	Catchments with 10% (or less) difference between observed and estimated *R*
R_1 (HYB-MPI)	220	55%
R_2 (HYB-GLEAM)	227	53%
R_3 (GPCC-MPI)	262	44%
R_4 (GPCC-GLEAM)	275	40%

water balance closes better when using data from HYBAM and MPI (7%) or HYBAM and GLEAM (10%). For data using GPCC and MPI or GPCC and GLEAM, deviations are 11% and 14%, respectively. However, the closure of the long-term water budget is not entirely guaranteed with these combinations of datasets for all the subcatchments, since only for 40% (with R4) and up to 55% (with R1) of them we could say that the water balance does close or that the temporal changes in storage can be considered negligible. This is shown in Table 2 and Figure 6, which presents the frequency of the relative differences and their ranges. This figure shows that for most subcatchments, runoff is better estimated using *P* from HYBAM and actual *E* from MPI. Also, there are seven subcatchments with imbalances equal to 80% or up. These imbalances seem to be due to great differences between precipitation datasets. From these seven subcatchments, four belong to the subbasin Madeira (south of the ARB) and three are located northeast, close to the mouth of the main Amazon River. For example, in the subcatchment *Serra Do Moa*, *P* from HYBAM is 1440 mm yr^{-1}, while *P* from GPCC is 2395 mm yr^{-1}; and for the subbasin Madeira (at Fazenda Vista Alegre), *P* from HYBAM is 1862 mm yr^{-1}, while *P* from GPCC is 2429 mm yr^{-1}. Given the location of the subcatchments (south of the ARB) and their runoff data, it seems that the GPCC dataset is overestimating *P* since both have low observed *R*.

Figure 7 shows the spatial distribution of runoff for each combination of datasets. Results show that regardless of the used model, all maps show a similar spatial pattern with the highest (lowest) runoff located in the northwestern (southern) region of the ARB. These results coincide with maps of precipitation (Fig. 2), indicating that regional runoff patterns in the ARB are driven mostly by precipitation distribution in the basin.

Results for the runoff sensitivity coefficients

Here, we perform an in-depth analysis of the runoff sensitivity coefficients in Eq. (5) and their constitutive terms (Eqs. 6–8) for each of the 100 subcatchments with runoff data, with the aim of quantifying relative changes in *R* as a function of relative changes in climate (*P* and E_p) and in the parameter *n*, using 12 different combinations of *P*, *E,* and E_p datasets in Table 1.

Table 3 shows the minimum, maximum, and mean values of the sensitivity coefficients calculated using long-term data for the ARB at its furthermost gauging station, Óbidos, and for the main six subbasins: Solimões, Negro, Purus, Madeira, Xingú, and Tapajós (Fig. 1). It also shows the standard deviation (SD) as a measure of the amount of variation or dispersion between 12 different combinations of datasets.

In summary, our results suggest that depending on the dataset combination, at Óbidos, a 10% increase in *P* would increase *R* between 15% and 17%, while a 10% increase in E_p would decrease *R* between 5% and 7%. In addition, a 10% change in factors embedded in the parameter *n* would affect the entire basin between 5% and 6%. Note that results presented in Table 3 evidence the water balance constraint[65] since ε_P is in all cases a unit higher than ε_{E_p} and thus, SDε_P = SDε_{E_p}.

Comparison between the six major subbasins in Table 3 shows that Madeira exhibits the highest differences between datasets, evidenced in its SD. In this subbasin, a 10% increase in *P* would increase *R* between 15% and 33%, a 10% increase in E_p would decrease *R* between 5% and 23%, and 10% change in the parameter *n* would affect the entire basin
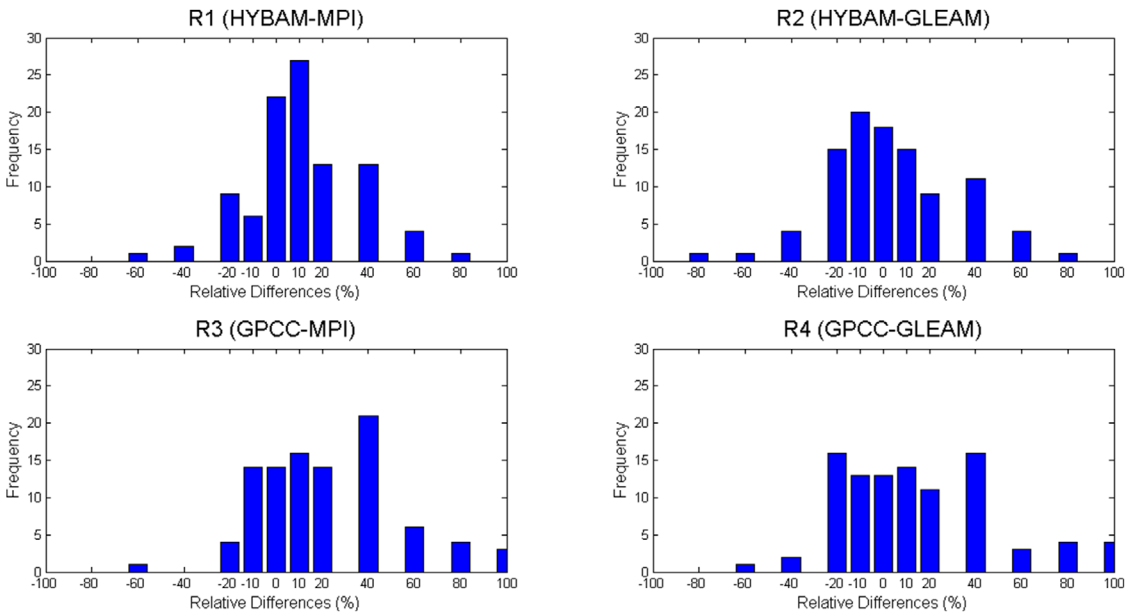
Figure 6. Histograms of relative differences between estimated and observed runoff for 100 subcatchments in the ARB.

between 2% and 7%. This subbasin was identified to be one with the highest imbalance in runoff estimation depending on the dataset.

Results at a smaller spatial scale (subcatchment scale) are presented in Figure 8. This figure shows the spatial variability of the mean value of the sensitivity coefficients (Fig. 8A and B) and their respective SD (Fig. 8C and D) for all the 100 subcatchments. Only maps for ε_P and ε_n are plotted given the water balance constraint between ε_P and ε_{E_p}, evidenced in Table 3. In Figure 8A and B, darker colors represent regions with higher values of both ε_P and ε_n. Thus, these regions are subcatchments in which changes in P (Fig. 8A) or in other factors that affect the partitioning of P (Fig. 8B) would affect runoff the most. Panels 8A and D show those regions in which there is a higher (lower) deviation from the results estimated using the different datasets, represented by their SD. Thus, those subcatchments have the highest uncertainty in the results. Regarding SD of ε_P, most of these subcatchments also belong to Madeira, located south of the ARB, coinciding with imbalances in water balance closure. As for uncertainty in ε_n, again higher values are evidenced toward the south (in Madeira) but also to the west near the Andes and to the northeast close to the mouth of the ARB.

Input data uncertainty of streamflow sensitivity

Next, we disentangle the different impacts of data uncertainty on the sensitivity coefficients ε_P and ε_n using Eqs. (9) and (11). We only show results for ε_P and ε_n, since results for ε_P and ε_{E_p} are the same given the aforementioned water balance constraint evidenced for the Amazon at Óbidos and the six main river basins in Table 2. Table 4 shows results of the relative contributions of P, E, and E_p to the sensitivity coefficients for the entire river basin (at Óbidos) and within the six main subbasins.

Table 4 shows that for the entire Amazon and its major subbasins, the relative contribution of actual E to the sensitivity of P is higher than the respective relative contribution of P and E_p. Also, regarding results for the sensitivity of factors embedded in n, ε_n, Table 4 shows that for the entire Amazon at Óbidos, the relative contribution of E_p to ε_n is higher than the contribution of P and E to ε_n. However, results vary from catchment to catchment. Spatial variability of the relative contribution of each variable to ε_p and ε_n for 100 subcatchments in the ARB is shown in Figure 9. This figure shows that at the subcatchment scale, relative contributions of E to ε_P (Fig. 9B) dominate the picture in the ARB, followed by the relative contribution of P to ε_P (Fig. 9A). On
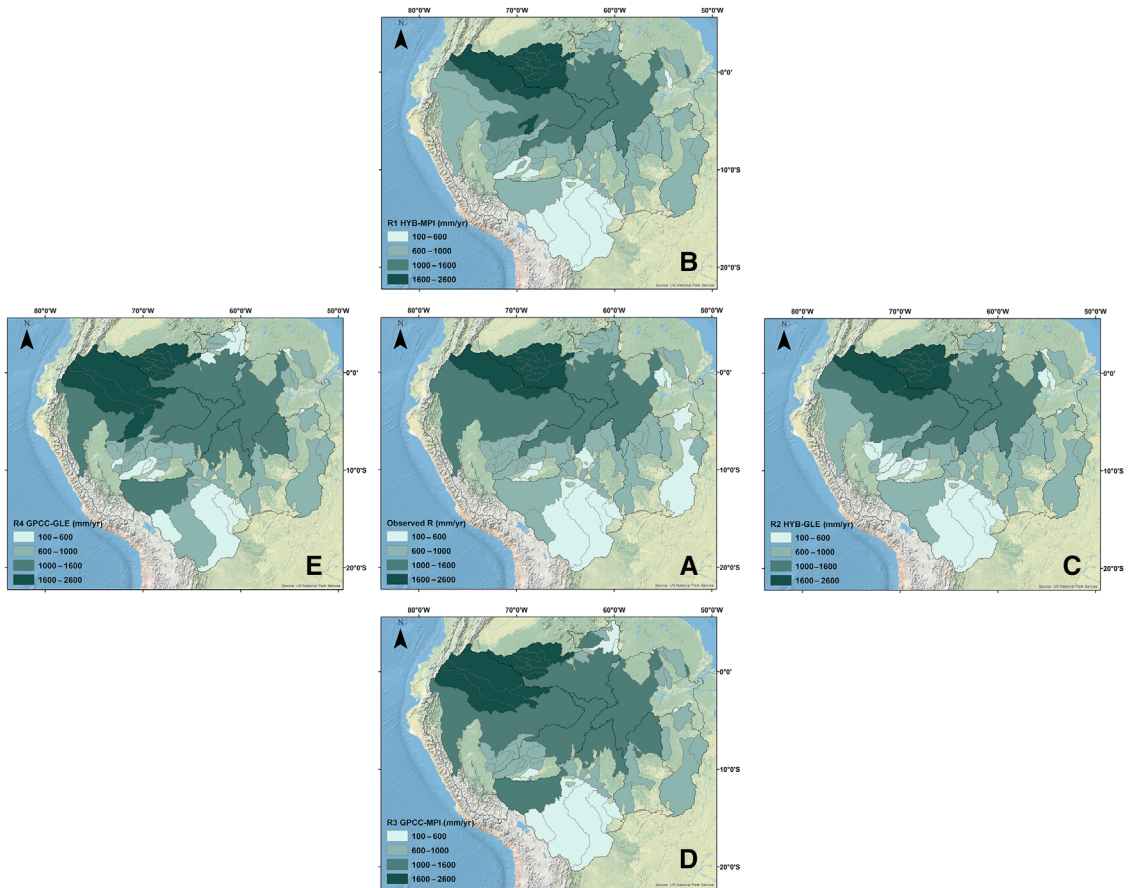
Figure 7. Comparison of spatial patterns of estimated *R* using four combinations of datasets of *P*, *E*, and observed *R*. Observed *R* is the middle of the figure (A) allowing for comparison with *R1* (B), *R2* (C), *R3* (D), and *R4* (E).

the other hand, in 62% of the subcatchments, the relative contribution of E_p to ε_n (Fig. 9F) is higher than the relative contribution of *P* to ε_n and *E* to ε_n.

Discussion

In this study, we analyze the implications of using different datasets and products to assess the relative changes in runoff *R* in the ARB, given relative changes in climatic variables (*P* and E_p), as well as in other properties that affect the partitioning of *P*, represented by *n*.

First, we study the variability of different datasets and products of *P*, actual *E*, and E_p and their regional distribution across the ARB. We show that all precipitation datasets exhibit similar regional patterns of *P* with the highest values of annual precipitation occurring in the Colombian Amazon (northwestern region), while the lowest precipita-

tion rates are depicted in Peru (western region), Bolivia (southwestern region), and some parts of Brazil (southeastern region). These observations coincide with macroclimatic factors, such as the migration of the Intertropical Convergence Zone (ITZC) and the South Atlantic Convergence Zone (SACZ), the activity of aerial rivers, and large-scale circulation patterns across South America,[70–74] including the Eastern Andean jet, also known as the Orinoco jet (northernmost leg of the SALJET),[75,76] and the two phases of the ENSO,[20,23,24] land surface–atmosphere interactions,[21,77–79] vegetation activity, and precipitation recycling.[80–82] Regarding E_p, we show that both E_p products produce quite different spatial results. The Hargreaves method locates the highest E_p values (of up to 1885 mm yr^{-1}) over the eastern part of the ARB decreasing westward, while the Priestley–Taylor estimates

Table 3. Results for the sensitivity coefficients in the Amazon River basin and its six major river basins

		Amazon (Óbidos)	Negro	Purus	Solimões	Madeira	Tapajós	Xingú
ε_p	Minimum	1.51	1.40	1.35	1.40	1.51	1.66	1.85
	Maximum	1.74	1.73	1.62	1.56	3.32	2.19	2.36
	Mean	1.64	1.56	1.50	1.49	2.06	1.83	2.04
	SD	0.08	0.10	0.10	0.06	0.62	0.17	0.19
ε_{E_p}	Minimum	0.51	0.40	0.35	0.40	0.51	0.66	0.85
	Maximum	0.74	0.73	0.62	0.56	2.32	1.19	1.36
	Mean	0.64	0.56	0.50	0.49	1.06	0.83	1.04
	SD	0.08	0.10	0.10	0.06	0.62	0.17	0.19
ε_n	Minimum	0.50	0.45	0.44	0.40	0.17	0.49	0.70
	Maximum	0.58	0.54	0.47	0.47	0.70	0.68	0.86
	Mean	0.53	0.49	0.46	0.44	0.52	0.58	0.74
	SD	0.02	0.03	0.01	0.03	0.20	0.07	0.05

locate the highest E_p values toward the northeast, decreasing systematically toward the southwest. The key difference is that we use remote sensing–based observations of surface net radiation for the Priestley–Taylor based estimate, whereas the often-used Hargreaves equation is solely based on daily average and diurnal temperature range data and extraterrestrial radiation. Thereby, the Hargreaves equation contains empirical coefficients that have been established at local scales and these may not be constant throughout the region. As for the results for actual E, the two datasets used, namely, MPI and GLEAM, produce different spatial patterns in the long-term mean annual actual E, and although both coincide in that the region with the lowest values of E appear to be near Perú and Bolivia. For comparison purposes in those subcatchments where Q data were available, E was also estimated using the water balance equation as $E = P–R$. Results show disagreement between remote sensing actual E and the water budget at the climatological mean.

Above, we attempted to estimate the closure of the water balance. Our results allow us to conclude that the closure of the long-term water budget is not entirely guaranteed with these combinations of datasets for all the subcatchments. Assuming that we accept a 10% difference between estimated and observed values of R for each subcatchment, for 40% and up to 55% of the subcatchments (depending on the combination of datasets), we could say that the water balance does close or that the changes in storage can be considered negligi-

ble. In the worst cases, these imbalances seemed to be driven by but not limited to differences in precipitation datasets. However, recalling the subsection "*Spatial availability of actual E*," there is a large discrepancy in climatological water budget–derived E and remote sensing–based estimates, since in about 45% of subcatchments, there are high relative differences between actual evapotranspiration datasets. Closing the water balance at a regional scale is most important to improve water resource assessment and its vulnerability to global change. However, it should be kept in mind that the water balance in a catchment may not close when all assumptions in Eq. (4) are not met. These assumptions include the requirement of long-term, high-quality hydrological measurements (over 20–30 years of data), negligible water storage changes from seasonal to interannual timescales, as well as contributions of groundwater net transport; and also, the stationary probability density functions of hydrological variables according to the mean value theorem.[83] For example, Miguez-Macho and Fan,[84] and Pokhrel *et al.*[85] explore the role of groundwater in the Amazon water cycle, finding large contributions of lateral groundwater exchange, while Frappart *et al.*[86] discuss large seasonal water storage, as derived from GRACE estimates in the northwestern region of the ARB. Also, historical trends in hydrological variables have been found in Amazonia. Data show increasing trends in temperature records,[87,88] while precipitation shows mixed evidence of increasing and
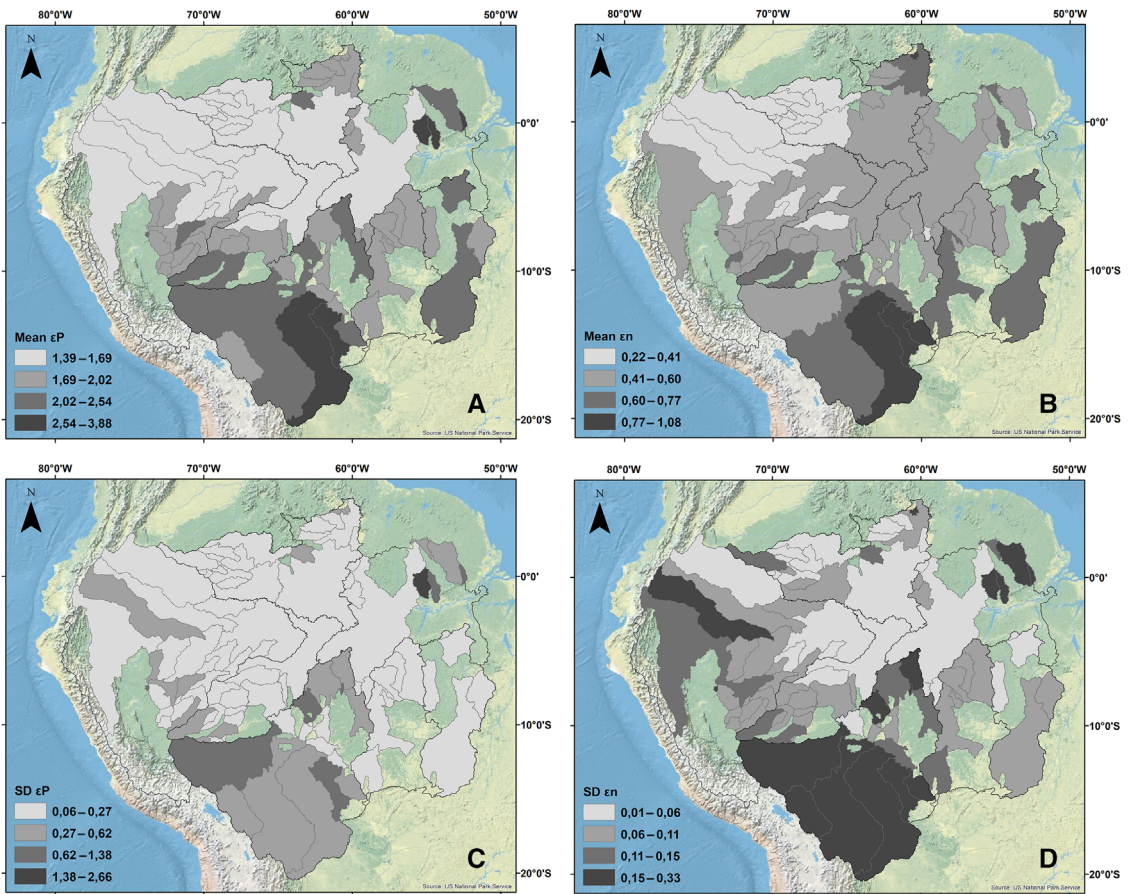
Figure 8. Spatial distribution of the mean value and the standard deviation (SD) of the sensitivity coefficients: sensitivity to *P* (A and C) and to *n* (B and D), respectively.

decreasing trends throughout the ARB.[89,90] Similarly, the mean and minimum river discharges exhibit decreasing trends in the Tapajós River, the upstream Madeira, and the Peruvian Amazon rivers. By contrast, increasing trends have been detected in mean and maximum river discharges in the northwestern Putumayo and Napo Rivers.[91] Thus, these possible signs of climate change in the ARB evidenced in trends in the long-term series might violate the assumption of stationarity.

Later on, following Roderick and Farquhar,[35] we quantified changes in *R* as a function of changes in climate (*P* and E_p) and in other factors represented by *n*, using the different combination of datasets of *E* and E_P. It is important to recall that the parameter *n* encompasses all factors that change the partitioning of *P* between evaporation and stream-

flow. Thus, it includes other climate characteristics, such as precipitation seasonality, timing, intensity, and form.[35,44,92–94] Specifically, as pointed out by Berghuijs and Woods,[94] disregarding the role of climate intraanual variability can bias the attribution of the parameter *n* toward landscape properties, prevents landscape effects from being strictly separated from intraanual climate effects, overestimates the importance of landscape effects, and ignores the role of a part of the climate effects on water yield.

Our results show that at Óbidos, the furthest downstream gauging station along the Amazon River, theoretical results suggest that depending on the dataset combination, a 10% increase in *P* would increase *R* between 15% and 17%, while a 10% increase in E_p would decrease *R* between 5% and 7%. In addition, a 10% change in *n* would affect
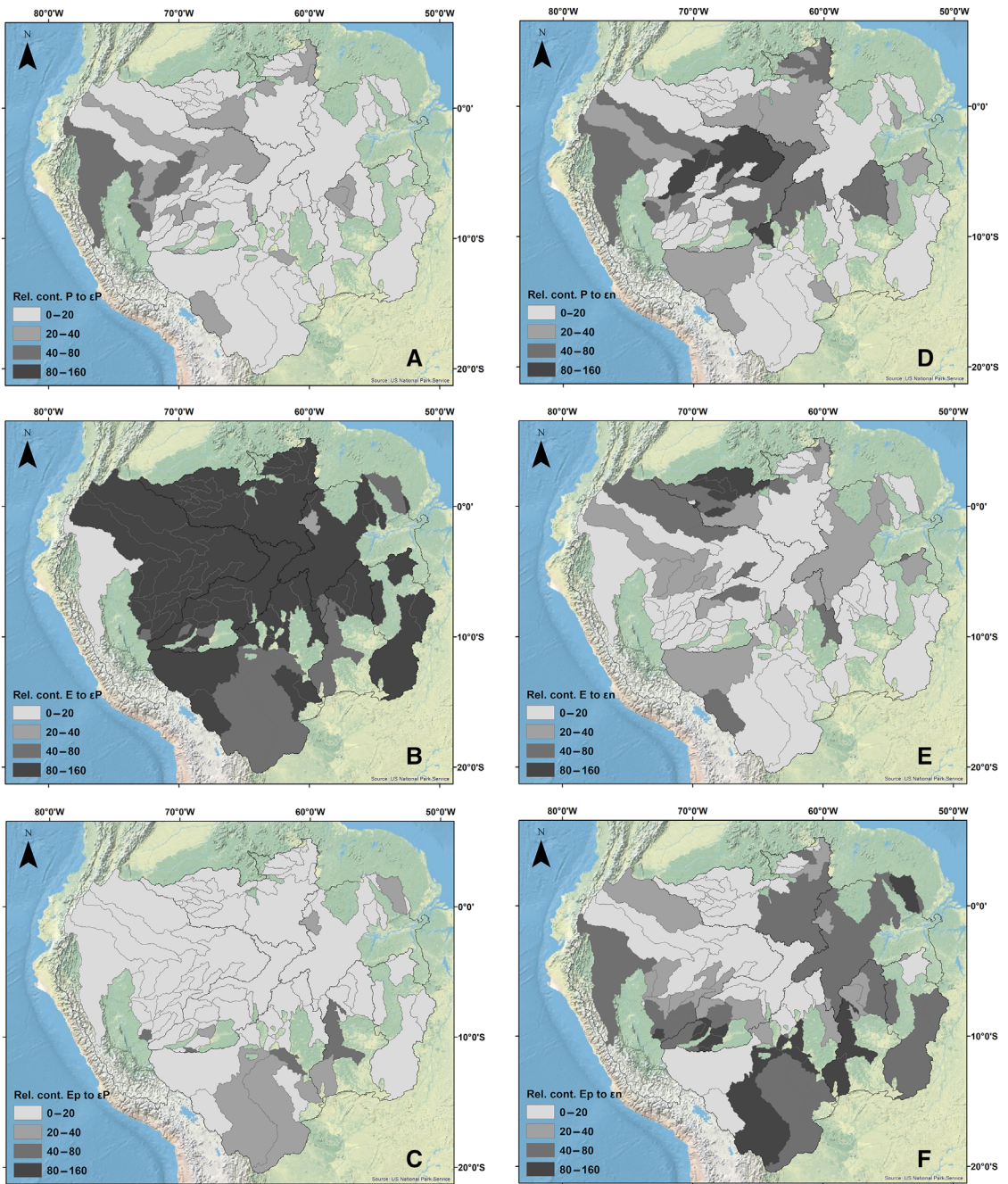
Figure 9. Relative contribution of *P*, *E*, and *E*$_p$ to the sensitivity coefficients ε_p (maps on the left: A–C) and ε_n (maps on the right: D–F).

the entire basin between 5% and 6%. Also, between the six major subbasins, Madeira exhibits the highest uncertainty in results, which could be related to its water closure imbalance identified above. Other regions with high differences between datasets in the sensitivity in catchment properties are located west near the Andes and to the northeast close to the mouth of the ARB.

Table 4. Relative contributions of *P*, *E*, and E_p for the sensitivity coefficients of the six major river basins within the ARB

River basin	P to ε_p (%)	E to ε_p (%)	E_p to ε_p (%)	P to ε_n (%)	E to ε_n (%)	E_p to ε_n (%)
Amazon (Óbidos)	3.4	91.26	2.69	3.16	26.19	58.49
Negro	10.41	103.82	1.86	24.43	12.31	51.69
Purus	1.77	100.84	0.02	69.16	14.39	0.00
Solimões	36.52	138.67	0.07	85.10	0.83	0.06
Madeira	6.49	112.89	0.01	43.60	27.52	0.00
Tapajós	15.05	113.59	3.01	61.76	1.47	41.35
Xingú	4.89	103.96	0.18	27.41	31.60	10.01

Finally, when estimating the relative contribution of each input variable to ε_P, and ε_n for 100 subcatchments in the ARB, results show that uncertainty of the sensitivity to climatic changes (ε_p) is dominated by the uncertainty in the catchment scale E. By contrast, the uncertainty of sensitivity of streamflow to changes in catchment properties ε_n is dominated by atmospheric demand and supply.

Our results show that in most regions of the ARB, either E or E_p, which showed most differences between datasets, dominates contributions in runoff sensitivity coefficients. On the other hand, there are also catchments in which uncertainty is due to differences in precipitation products, evidenced in the imbalance of the water balance closure. Thus, we show that using diverse combinations of datasets can lead to different results with implications for the quantification of climate change impacts at the subcatchment scale in the ARB. Specifically, our results suggest that in order to improve our understanding of the possible future scenarios of hydrological sensitivity, enhanced estimates of E and E_p are needed since uncertainties in E seem to dominate over the uncertainties in P in the ARB.

Acknowledgments

Competing interests

The authors declare no competing interests.

References

1. Lenton, T.M., H. Held, E. Kriegler, *et al.* 2008. Tipping elements in the Earth's climate system. *Proc. Natl. Acad. Sci. USA* **105:** 1786–1793.
2. Lenton, T.M., J. Rockström, O. Gaffney, *et al.* 2019. Climate tipping points—too risky to bet against. *Nature* **575:** 592–595.
3. Lovejoy, T.E. & C. Nobre. 2018. Amazon tipping point. *Sci. Adv.* **4:** eaat2340.
4. Zemp, D.C., C.F. Schleussner, H.M. Barbosa, *et al.* 2017. Self-amplified Amazon forest loss due to vegetation–atmosphere feedbacks. *Nat. Commun.* **8:** 1–10.
5. Staal, A., B.M. Flores, A.P.D. Aguiar, *et al.* 2020. Feedback between drought and deforestation in the Amazon. *Environ. Res. Lett.* **15:** 044024.
6. Oyama, M.D. & C.A. Nobre. 2003. A new climate-vegetation equilibrium state for tropical South America. *Geophys. Res. Lett.* **30**. https://doi.org/10.1029/2003GL018600
7. Senna, M.C.A., M.H. Costa & G.F. Pires. 2009. Vegetation-atmosphere-soil nutrient feedbacks in the Amazon for different deforestation scenarios. *J. Geophys. Res. Atmos.* **114**. https://doi.org/10.1029/2008JD010401
8. Nobre, C.A. & L.D.S. Borma. 2009. 'Tipping points' for the Amazon forest. *Curr. Opin. Environ. Sustain.* **1:** 28–36.
9. Salazar, L.F. & C.A. Nobre. 2010. Climate change and thresholds of biome shifts in Amazonia. *Geophys. Res. Lett.* **37**. https://doi.org/10.1029/2010GL043538
10. Hirota, M., M. Holmgren, E.H. Van Nes & M. Scheffer. 2011. Global resilience of tropical forest and savanna to critical transitions. *Science* **334:** 232–235.
11. Pires, G.F. & M.H. Costa. 2013. Deforestation causes different subregional effects on the Amazon bioclimatic equilibrium. *Geophys. Res. Lett.* **40:** 3618–3623.
12. Nobre, C.A., G. Sampaio, L.S. Borma, *et al.* 2016. Land-use and climate change risks in the Amazon and the need of a novel sustainable development paradigm. *Proc. Natl. Acad. Sci. USA* **113:** 10759–10768.
13. Boers, N., N. Marwan, H.M. Barbosa & J. Kurths. 2017. A deforestation-induced tipping point for the South American monsoon system. *Sci. Rep.* **7:** 41489.
14. Ciemer, C., N. Boers, M. Hirota, *et al.* 2019. Higher resilience to climatic disturbances in tropical vegetation exposed to more variable rainfall. *Nat. Geosci.* **12:** 174–179.

15. Salazar, J.F., J.C. Villegas, A.M. Rendón & E. Rodríguez. 2018. Scaling properties reveal regulation of river flows in the Amazon through a "forest reservoir." *Hydrol. Earth Syst. Sci.* **22:** 1735–1748.

16. Builes-Jaramillo, A. & G. Poveda. 2018. Conjoint analysis of surface and atmospheric water balances in the Andes-Amazon system. *Water Resour. Res.* **54:** 3472–3489.

17. Greve, P., L. Gudmundsson, B. Orlowsky & S. Seneviratne. 2015. The Budyko framework beyond stationarity. *Hydrol. Earth Syst. Sci. Discuss.* **12:** 6799–6830.

18. Moussa, R., J.P. Lhomme & L. Gudmundsson. 2016. The Budyko functions under non-steady-state conditions. *Hydrol. Earth Syst. Sci.* **20:** 4867–4879.

19. Guimberteau, M., P. Ciais, A. Ducharne, *et al.* 2017. Impacts of future deforestation and climate change on the hydrology of the Amazon Basin: a multi-model analysis with a new set of land-cover change scenarios. *Hydrol. Earth Syst. Sci.* **21:** 1455–1475.

20. Marengo, J.A. 1992. Interannual variability of surface climate in the Amazon basin. *Int. J. Climatol.* **12:** 853–863.

21. Poveda, G. & O.J. Mesa. 1997. Feedbacks between hydrological processes in tropical South America and large scale oceanic atmospheric phenomena. *J. Clim.* **10:** 2690–2702.

22. Ronchail, J., G. Cochonneau, M. Molinier, *et al.* 2002. Interannual rainfall variability in the Amazon basin and sea-surface temperatures in the equatorial Pacific and the tropical Atlantic Oceans. *Int. J. Climatol.* **22:** 1663–1686.

23. Schöngart, J. & W.J. Junk. 2007. Forecasting the flood-pulse in Central Amazonia by ENSO-indices, *J. Hydrol.* **335:** 1–2.

24. Jiménez-Muñoz, J.C., C. Mattar, J. Barichivich, *et al.* 2016. Record-breaking warming and extreme drought in the Amazon rainforest during the course of El Niño 2015–2016. *Sci. Rep.* **6:** 33130.

25. Sposito, G. 2017. Understanding the Budyko equation. *Water* **9:** 236.

26. Cai, W., M.J. McPhaden, A.M. Grimm, *et al.* 2020. Climate impacts of the El Niño–Southern oscillation on South America. *Nat. Rev. Earth Environ.* **1:** 215–231.

27. Builes-Jaramillo, A., N. Marwan, G. Poveda & J. Kurths. 2018. Nonlinear interactions between the Amazon River basin and the Tropical North Atlantic at interannual timescales. *Clim. Dyn.* **50:** 2951.

28. Yoon, J.H. & N. Zeng. 2010. An Atlantic influence on Amazon rainfall. *Clim. Dyn.* **34:** 249.

29. Marengo, J.A., C.A. Nobre, J. Tomasella, *et al.* 2008. The drought of Amazonia in 2005. *J. Clim.* **21:** 495–516.

30. Arora, V.K. 2002. The use of the aridity index to assess climate change effect on annual runoff. *J. Hydrol.* **265:** 164–177.

31. Ma, Z., S. Kang, L. Zhang, *et al.* 2008. Analysis of impacts of climate variability and human activity on streamflow for a river basin in arid region of northwest china. *J. Hydrol.* **352:** 239–249.

32. Zhang, L., N. Potter, K. Hickel, *et al.* 2008. Water balance modeling over variable time scales based on the Budyko framework—model development and testing. *J. Hydrol.* **360:** 117–131.

33. Renner, M. & C. Bernhofer. 2011. Applying simple water–energy balance frameworks to predict the climate sensitiv-

34. Renner, M., R. Seppelt & C. Bernhofer. 2012. Evaluation of water–energy balance frameworks to predict the sensitivity of streamflow to climate change. *Hydrol. Earth Syst. Sci.* **16:** 1419–1433.

35. Roderick, M. & G. Farquhar. 2011. A simple framework for relating variations in runoff to variations in climatic conditions and catchment properties. *Water Resour. Res.* **47.** https://doi.org/10.1029/2010WR009826

36. Wang, D. & M. Hejazi. 2011. Quantifying the relative contribution of the climate and direct human impacts on mean annual streamflow in the contiguous United States. *Water Resour. Res.* **47.** https://doi.org/10.1029/2010WR010283

37. Blöschl, G., M. Sivapalan, T. Wagener, *et al.* 2013. *Runoff Prediction in Ungauged Basins: Synthesis Across Processes, Places and Scales*. Cambridge: Cambridge University Press, 490 p.

38. Renner, M., K. Brust, K. Schwärzel, *et al.* 2014. Separating the effects of changes in land cover and climate: a hydrometeorological analysis of the past 60 yr in Saxony, Germany. *Hydrol. Earth Syst. Sci.* **18:** 389–405.

39. Carmona, A., G. Poveda, M. Sivapalan, *et al.* 2016. A scaling approach to Budyko's framework and the complementary relationship of evapotranspiration in humid environents: case study of the Amazon River basin. *Hydrol. Earth Syst. Sci.* **20:** 589–603.

40. Hasan, E. *et al.* 2018. Runoff sensitivity to climate change in the Nile River Basin. *J. Hydrol.* **561:** 312–321.

41. Lv, X., Z. Zuo, Y. Ni, *et al.* 2019. The effects of climate and catchment characteristic change on streamflow in a typical tributary of the Yellow River. *Sci. Rep.* **9:** 14535.

42. Li, Y., C. Liu, W. Yu, *et al.* 2019. Response of streamflow to environmental changes: a Budyko-type analysis based on 144 river basins over China. *Sci. Total Environ.* **664:** 824--833.

43. Zhang, X. *et al.* 2019. A Budyko-based framework for quantifying the impacts of aridity index and other factors on annual runoff. *J. Hydrol.* **579.** https://doi.org/10.1016/j.jhydrol.2019.124224

44. Milly, P. 1994. Climate, soil water storage, and the average annual. *Water Resour. Res.* **30:** 2143–2156.

45. Koster, R. & M. Suarez. 1999. A simple framework for examining the interannual variability of land surface moisture fluxes. *J. Clim.* **12:** 1911–1917.

46. Zhang, L., W. Dawes & G. Walker. 2001. Response of mean annual evapotranspiration to vegetation changes at catchment scale. *Water Resour. Res.* **37:** 701–708.

47. Yang, D., F. Sun, Z. Liu, *et al.* 2007. Analyzing spatial and temporal variability of annual water–energy balance in non-humid regions of China using the Budyko hypothesis. *Water Resour. Res.* **43:** 1–12.

48. Donohue, R., M. Roderick & T. McVicar. 2007. On the importance of including vegetation dynamics in Budyko's hydrological model. *Hydrol. Earth Syst. Sci.* **11:** 983–995.

49. Sposito, G. 2017. Incorporating the vadose zone into the Budyko framework. *Water* **9:** 698.

50. Rouholahnejad Freund, E. & J.W. Kirchner. 2017. A Budyko framework for estimating how spatial heterogeneity and

lateral moisture redistribution affect average evapotranspi-
ration rates as seen from the atmosphere. *Hydrol. Earth Syst.
Sci.* **21:** 217–233.

51. Molinier, M., J. Guyot, E. De Oliveira & V. Guimarães. 1996.
Les Regimes Hydroiogiques De l'Amazone Et De Ses Affluents.
IAHS Publication. 209–222.

52. Salazar, J. 2004. Water balances and extreme discharge esti-
mation in Amazonia (in Spanish). Masters Thesis. Universi-
dad Nacional de Colombia, Sede Medellín.

53. Schneider, U., A. Becker, A. Meyer-Christoffer, *et al.*
2011. Global precipitation analysis products of the GPCC.
Global Precipitation Climatology Centre (GPCC), DWD.
12 pp. Accessed December 2017. https://www.dwd.de/EN/
ourservices/gpcc/gpcc.html.

54. Jung, M., M. Reichstein, P. Ciais, *et al.* 2010. Recent decline
in the global land evapotranspiration trend due to limited
moisture supply. *Nature* **467:** 951–954.

55. Miralles, D.G., T.R.H. Holmes, R.A.M. de Jeu, *et al.* 2011.
Global land-surface evaporation estimated from satellite-
based observations. *Hydrol. Earth Syst. Sci.* **15:** 453–
469.

56. Martens, B., D.G. Miralles, H. Lievens, *et al.* 2017. GLEAM
v3: satellite-based land evaporation and root-zone soil mois-
ture. *Geosci. Model Dev.* **10:** 1903–1925.

57. Hargreaves, G.H. & Z.A. Samani. 1982. Estimating poten-
tial evapotranspiration. *J. Irrig. Drain. Div.* **108:** 225–
230.

58. Trabucco, A. & R. Zomer. 2009. Global aridity index (global-
aridity) and global potential evapotranspiration (global-pet)
geospatial database. CGIAR Consortium for Spatial Infor-
mation. Accessed December 2017. Available from the
CGIAR-CSI GeoPortal at http://www.csi.cgiar.org/(2009).
The new dataset is available at https://figshare.com/articles/
Global_Aridity_Index_and_Potential_Evapotranspiration_
ET0_Climate_Database_v2/7504448/3.

59. Jones, P.D., D.H. Lister, T.J. Osborn, *et al.* 2012. Hemispheric
and large-scale land surface air temperature variations: an
extensive revision and an update to 2010. *J. Geophys. Res.*
117: D5.

60. Priestley, C.H.B. & R.J. Taylor. 1972. On the assessment
of the surface heat flux and evaporation using large-scale
parameters. *Mon. Weather Rev.* **100:** 81–92.

61. Cox, S.J., P.W. Stackhouse, Jr., S.K. Gupta, *et al.* 2017.
NASA/GEWEX shortwave surface radiation budget: inte-
grated data product with reprocessed radiance, cloud, and
meteorology inputs, and new surface albedo treatment. In
AIP Conference Proceedings (Vol. 1810, No. 1, p. 090001).
AIP Publishing LLC.

62. Dooge, J.C.I. 1982. Parameterization of hydrologic pro-
cesses. In *Land Surface Processes in Atmospheric General
Circulation Models*. P.S. Eagleson, Ed.: 243–288. Cambridge
University Press.

63. Eagleson, P.E. 1994. The evolution of modern hydrology
(from watershed to continent in 30 years). *Adv. Water Res.*
17: 3–18.

64. Budyko, M. 1974. *Climate and Life*. Orlando: Academic
Press. 508 p.

65. Kuhnel, V., J.C.I. Dooge, J.P.J. O'Kane & R.J. Romanowicz.
1991. Partial analysis applied to scale problems in surface
moisture fluxes. *Surv. Geophys.* **12:** 221–247.

66. Yang, H. & D. Yang. 2011. Derivation of climate elasticity
of runoff to assess the effects of climate change on annual
runoff. *Water Resour. Res.* **47:** W07526.

67. Yang, H., D. Yang, Z. Lei & F. Sun. 2008. New analytical
derivation of the mean annual water–energy balance equa-
tion. *Water Resour. Res.* **44:** W03410.

68. Jung, M., M. Reichstein, C.R. Schwalm, *et al.* 2017. Compen-
satory water effects link yearly global land CO_2 sink changes
to temperature. *Nature* **541:** 516.

69. Kummerow, C., W. Barnes, T. Kozu, *et al.* 1998. The Tropi-
cal Rainfall Measuring Mission (TRMM) Sensor Package. *J.
Atmos. Oceanic Technol.* **15:** 809–817.

70. Poveda, G., L. Jaramillo & L.F. Vallejo. 2014. Seasonal precip-
itation patterns along pathways of South American low-level
jets and aerial rivers. *Water Resour. Res.* **50:** 98–118.

71. Moraes-Arraut, J., C.A. Nobre, H.M. Barbosa, *et al.* 2012.
Aerial rivers and lakes: looking at large-scale moisture
transport and its relation to Amazonia and to subtropical
rainfall in South America. *J. Clim.* **25:** 543–556.

72. Paccini, L., J.C. Espinoza, J. Ronchail & H. Segura. 2018.
Intra-seasonal rainfall variability in the Amazon basin
related to large-scale circulation patterns: a focus on western
Amazon–Andes transition region. *Int. J. Climatol.* **38:** 2386–
2399.

73. Espinoza, J.C., R. Garreaud, G. Poveda, *et al.* 2020. Hydrocli-
mate of the Andes Part I: main climatic features. *Front. Earth
Sci.* **8.** https://doi.org/10.3389/feart.2020.00064

74. Poveda, G., J.C. Espinoza, M.D. Zuluaga, *et al.* 2020. High
impact weather events in the Andes. *Front. Earth Sci.* **8.**
https://doi.org/10.3389/feart.2020.00162

75. Montoya, G., J. Pelkowski & J.A. Eslava. 2001. On the north-
east trade winds and the existence of a current along the
eastern Andean piedmont (in Spanish). *Rev. Acad. Colomb.
Cienc.* **96:** 363–370.

76. Jiménez-Sánchez, G., P.M. Markowski, V. Jewtoukoff, *et al.*
2019. The Orinoco low-level jet: an investigation of its char-
acteristics and evolution using the WRF model. *J. Geophys.
Res. Atmos.* **124:** 10696–10711.

77. Levine, P.A., J.T. Randerson, Y. Chen, *et al.* 2019. Soil mois-
ture variability intensifies and prolongs eastern Amazon
temperature and carbon cycle response to El Niño–Southern
oscillation. *J. Clim.* **32:** 1273–1292.

78. Gentine, P., A. Massmann, B.R. Lintner, *et al.* 2019. Land–
atmosphere interactions in the tropics. *Hydrol. Earth Syst.
Sci. Discuss.* **23:** 4171–4197.

79. Bedoya-Soto, J.M., G. Poveda & D. Sauchyn. 2018. New
insights on land–atmosphere feedbacks over Tropical South
America at interannual timescales. *Water* **10.** https://doi.
org/10.3390/w10081095.

80. Zemp, D.C., C.-F. Schleussner, H.M.J. Barbosa, *et al.* 2014.
On the importance of cascading moisture recycling in South
America. *Atmos. Chem. Phys.* **14:** 13337–13359.

81. Molina, R.D., J.F. Salazar, J.A. Martínez, *et al.* 2019.
Forest-induced exponential growth of precipitation along

climatological wind streamlines over the Amazon. *J. Geoph. Res.: Atmos.* **124:** 2589–2599.

82. Eltahir, E. & R. Bras. 1994. Precipitation recycling in the Amazon basin. *Quart. J. Roy. Meteor. Soc.* **120:** 861–880.

83. Poveda, G., J.I. Vélez, O.J. Mesa, *et al.* 2007. Linking long-term water balances and statistical scaling to estimate river flows along the drainage network of Colombia. *J. Hydrol. Eng.* **12:** 4–13.

84. Miguez-Macho, G. & Y. Fan. 2012. The role of groundwater in the Amazon water cycle: 1. Influence on seasonal stream-flow, flooding and wetlands. *J. Geophys. Res. Atmos.* **117.** https://doi.org/10.1029/2012JD017539

85. Pokhrel, Y.N., Y. Fan, G. Miguez-Macho, *et al.* 2013. The role of groundwater in the Amazon water cycle: 3. Influence on terrestrial water storage computations and comparison with GRACE. *J. Geophys. Res. Atmos.* **118:** 3233–3244.

86. Frappart, F., F. Papa, A. Güntner, *et al.* 2011. Satellite-based estimates of groundwater storage variations in large drainage basins with extensive floodplains. *Remote Sens. Environ.* **115:** 1588–1594.

87. Victoria, R., L. Martinelli, J. Moraes, *et al.* 1998. Surface air temperature variations in the Amazon region and its borders during this century. *J. Clim.* **11:** 1105–1110.

88. Marengo, J., C. Nobre, R. Betts, *et al.* 2009. Global warming and climate change in Amazonia: climate–vegetation feedback and impacts on water resources. *Amazonia Glob. Change* **186:** 273–292.

89. Marengo, J. 2004. Interdecadal variability and trends of rainfall across the Amazon basin. *Theor. Appl. Climatol.* **78:** 79–96.

90. Carmona, A. & G. Poveda. 2011. Detection of long-term trends in monthly hydro-climatic records of Colombia and the Amazon River basin through empirical mode decomposition. In *AGU Fall Meeting Abstracts*, volume 1.

91. Espinoza, J., J. Ronchail, J. Guyot, *et al.* 2009. Spatio-temporal rainfall variability in the Amazon basin countries (Brazil, Peru, Bolivia, Colombia, and Ecuador). *Int. J. Climatol.* **29:** 1574–1594.

92. Berghuijs, W.R., R.A. Woods & M. Hrachowitz. 2014. A pre-cipitation shift from snow towards rain leads to a decrease in streamflow. *Nat. Clim. Change* **4:** 583–586.

93. Berghuijs, W.R., M. Sivapalan, R.A. Woods & H.H.G. Savenije. 2014. Patterns of similarity of seasonal water balances: a window into streamflow variability over a range of time scales. *Water Resour. Res.* **50:** 5638–5661.

94. Berghuijs, W.R. & R.A. Woods. 2016. Correspondence: space–time asymmetry undermines water yield assessment. *Nat. Commun.* **7:** 1–2.